This manuscript is a non-peer reviewed preprint that has been submitted to “Elementa: Science of the Anthropocene”.

Spatio-temporal variability of small-scale leads based on helicopter winter sea ice surface temperatures

Linda Thielke[1], Gunnar Spreen[1*], Marcus Huntemann[1], Dmitrii Murashkin[2,1]

[1]University of Bremen, Institute of Environmental Physics, Bremen, 28359, Germany

[2]German Aerospace Center (DLR), Remote Sensing Technology Institute (IMF), Bremen, Germany

*Corresponding author: gunnar.spreen@uni-bremen.de

Spatio-temporal variability of small-scale leads based on helicopter winter sea ice surface temperatures

Linda Thielke[1], Gunnar Spreen[1*], Marcus Huntemann[1], Dmitrii Murashkin[2,1]

[1]University of Bremen, Institute of Environmental Physics, Bremen, 28359, Germany

[2]German Aerospace Center (DLR), Remote Sensing Technology Institute (IMF), Bremen, Germany

[*]Corresponding author: gunnar.spreen@uni-bremen.de

Abstract

Surface temperature is crucial in studying the Arctic climate, particularly during winter. We examine 1 m resolution surface temperature maps of 35 helicopter flights between 02 October 2019 and 23 April 2020, recorded during the Multidisciplinary drifting Observatory for the Study of Arctic Climate (MOSAiC). The seasonal cycle of the average surface temperature spans from 265.6 K on 02 October 2019 to 231.8 K on 28 January 2020. The surface temperature is affected by atmospheric changes and also varies across scales. Furthermore, we concentrate on leads in sea ice because they allow for greater heat exchange between ocean and atmosphere than thick, snow-covered ice. Leads, which appear considerably warmer than sea ice, are classified by a temperature threshold. The local scale (5–10 km) lead area fraction varies between 0% and 4% with a higher variability than on a regional scale (20–40 km), where leads cover a more stable fraction of 0-1% until mid-January when it increases to 4%. The variability in the lead area is caused by sea ice dynamics (opening and closing of leads), as well as thermodynamics with ice growth (lead closing). To understand better the ice rheology throughout the winter, we identify lead orientation distributions. We find that the orientation varies between different flights but the distribution mostly shows one prominent orientation peak. Thus, we are not able to determine predominant intersection angles, which would need two modes in the orientation distribution. The lead width distribution follows a power law with a negative exponent of 2.63, which agrees with literature values, proves the comparability to other datasets, and extends the existing relationship to the smaller scales, as observed here. The appearance of many more small leads

compared to wider leads is important since they only occur on the sub-footprint scale of thermal infrared satellite data. Sub-satellite-footprint lead statistics are essential for Arctic-climate investigations because the ocean-atmosphere heat exchange does not scale linearly with lead area fraction and is larger for smaller leads.

1. Introduction

This study presents the spatio-temporal evolution of the Arctic sea ice surface temperature and lead area fraction, as well as the lead width and intersection angle. In this analysis, we refer to fractures in the sea ice cover like cracks and leads (>50 m width according to the definition of the World Meteorological Organization (WMO), (WMO, 2014)), jointly as ”leads”. The helicopter-borne surface temperature measurements were taken as part of the Multidisciplinary drifting Observatory for the Study of Arctic Climate (MOSAiC) in the central Arctic (Shupe et al., 2020). The MOSAiC expedition (Sep 2019–Oct 2020) allowed us to collect in-situ measurements from the central Arctic over a whole seasonal cycle for different aspects of the Arctic system (Nicolaus et al., 2022; Rabe et al., 2022; Shupe et al., 2022). Our measurement program was part of the sea ice and remote sensing teams (Nicolaus et al., 2022), which conducted a large collection of data from sea ice physics, on-ice remote sensing, over albedo, to snow properties. The analysis is based on data from 35 helicopter survey flights between October 2019 to April 2020, recorded with an infrared camera over the same ice floe and surrounding regions along the Transpolar Drift.

The investigation of sea ice processes is crucial for studying climate warming, which is especially strong in the high latitudes (Arctic Amplification) (Serreze and Barry, 2011; Wendisch et al., 2017; Dai et al., 2019; Masson-Delmotte et al., 2021). The warming is even stronger in winter than in summer, related to the feedbacks of infrared (IR) radiation in winter and ice-albedo during summer (Bintanja and Van Der Linden, 2013). Sea ice becomes significantly thinner (Meredith et al., 2019; Masson-Delmotte et al., 2021) with an average reduction of 2 m from the period 1958-1976 (submarine record) to the current altimeter period with strongest thinning during the ICESat period (2003-2008) (Kwok, 2018). With the decline in annual sea ice minimum extent in late summer, also the multiyear ice area has strongly decreased (Kwok, 2018). The thinner ice makes the sea ice more susceptible to wind and ocean current forcing, resulting in higher ice drift speeds (Spreen et al., 2011; Kwok et al., 2013). Rampal et al. (2009) hypothesizes that thinner sea ice has less mechanical strength, allowing easier breaking of the sea ice. The changing sea ice conditions influence the heat exchange between ocean and atmosphere, which is important for the whole Earth's Climate System and not only the Arctic regions (Serreze et al., 2009; Meredith et al., 2019). Leads and thin ice are much warmer than the surrounding sea ice and snow and thus heat loss is more than a magnitude larger in leads compared to the surrounding ice (Maykut, 1982). Therefore, a better understanding of the interaction between ocean, sea ice, and atmosphere is essential. The high resolution lead data presented here have the potential for evaluation of the sub-footprint scale information of satellite remote sensing products.

Leads, with open water or thin ice cover, have high variability in time and space (Yu and Rothrock, 1996; Willmes and Heinemann, 2015). Therefore, it is important to monitor their conditions throughout the year. In Arctic pack ice during winter, a lead area fraction (open water and thin ice combined) of less than 10% can be expected (Yu and Rothrock, 1996), while in the Central Arctic lead area fractions are typically even lower (Wang et al., 2016). Willmes and Heinemann (2016) (2003–2015; satellite) and Wang et al. (2016) (1985–2014; model) could not find a trend in the lead area fraction, and Wang et al. (2016) found that the winds mainly determine the inter-annual variability in lead area fraction. However, a precise determination of the lead area fraction is crucial. Lüpkes et al. (2008) showed that a slight change in the high sea ice concentration (SIC) range, e.g., by the opening of leads, affects the near-surface air temperature. According to their study, a change of 1% in SIC could cause an air temperature change of up to 3.5 K. Small reductions in SIC, mostly induced by leads, have a (non-linear) more efficient effect on the heat exchange between the ocean and atmosphere than when a closed sea ice cover is present (Maykut, 1978). Therefore small changes in winter sea ice concentration, i.e., changes in lead area fraction are necessary to monitor. For example, if an increase of surface temperature on regional scale (e.g. satellite footprint) is (i) caused by many small leads the heat flux is stronger affected than if it is (ii) caused by a thinner but closed ice cover.

We first describe our helicopter measurement program and explain the principles of thermal sea ice observation. In the next part, we describe the spatio-temporal variability of our high resolution surface temperatures. Afterwards, we describe the lead classification based on the temperature difference. In the next section, we analyse the temporal variability of the surface temperature and lead area fraction on different spatial scales and present a case study of the November 2019 storm event. The last part focuses on the lead properties, i.e., width and orientation, derived after segmenting the classified leads.

2. Data

2.1. *Thermal sea ice observation*

With an infrared camera (InfraTec VarioCAM HD) installed, 35 helicopter flights were performed on a roughly weekly basis between 02 October 2019 and 23 April 2020 from RV Polarstern (Alfred-Wegener-Institut Helmholtz-Zentrum für Polar- und Meeresforschung, 2017) (Figure 1). The set of flights consists of four main flight patterns: (i) Central Observatory (CO) (local), (ii) L-site triangles (regional), (iii) L-site grids (other), and (iv) event-related (other), like mapping particular leads. Detail about the surface temperature maps (Thielke et al., 2022) and pre-processing are presented in Thielke et al. (2022). To our knowledge regional scale sea ice infrared imaging has not yet been analysed and published before, such as done in the scope of this study.

Our measurements with helicopter-borne thermal infrared (TIR) imaging provide temperatures of the sea ice surface with a high spatial resolution of 1 m which is substantially higher than TIR satellites, like MODIS, that have a resolution of about 1 km. Nevertheless, satellites are the primary tool for the Arctic sea ice state observations (Spreen and Kern, 2017; Fox-Kemper et al., 2021). Compared to pan-Arctic coverage from satellites, we can provide with our helicopter data restricted area coverage from a local 5 km scale to a regional 40 km scale. Investigating the small-scale variability is important to better understand the representation of sea ice properties in models and satellite retrievals on a sub-grid scale (Vihma et al., 2014). Thus, this data is valuable for evaluating models and satellite retrievals (Ivanova et al., 2016).

The TIR temperature can distinguish open water and thin ice from thick ice, particularly for thin ice thickness of less than 1 m (Shokr and Sinha, 2015). Open water rarely exists in winter because the freezing starts directly after a lead opening. Therefore, we expect to capture mainly thin ice and only small open water areas with significantly warmer surface temperatures. Open water and thin ice areas influence the Arctic heat budget by allowing increased heat exchange between the ocean and the atmosphere. Above 1 m ice thickness, heat flux changes are minimal and have minor relevance for the Arctic heat budget (Maykut, 1982). Maykut (1982) found that in winter, the heat contribution from thin ice in leads is similar to the open water area and even larger than the dominating thick ice area.

The radiation in the TIR spectral region has a very small penetration depth on a sub-millimeters scale in snow, and ice (Shokr and Sinha, 2015, pages 272,294). As a result, the TIR brightness temperature provides a measurement of the upper surface of snow or sea ice. Thus, the recorded temperature is expected

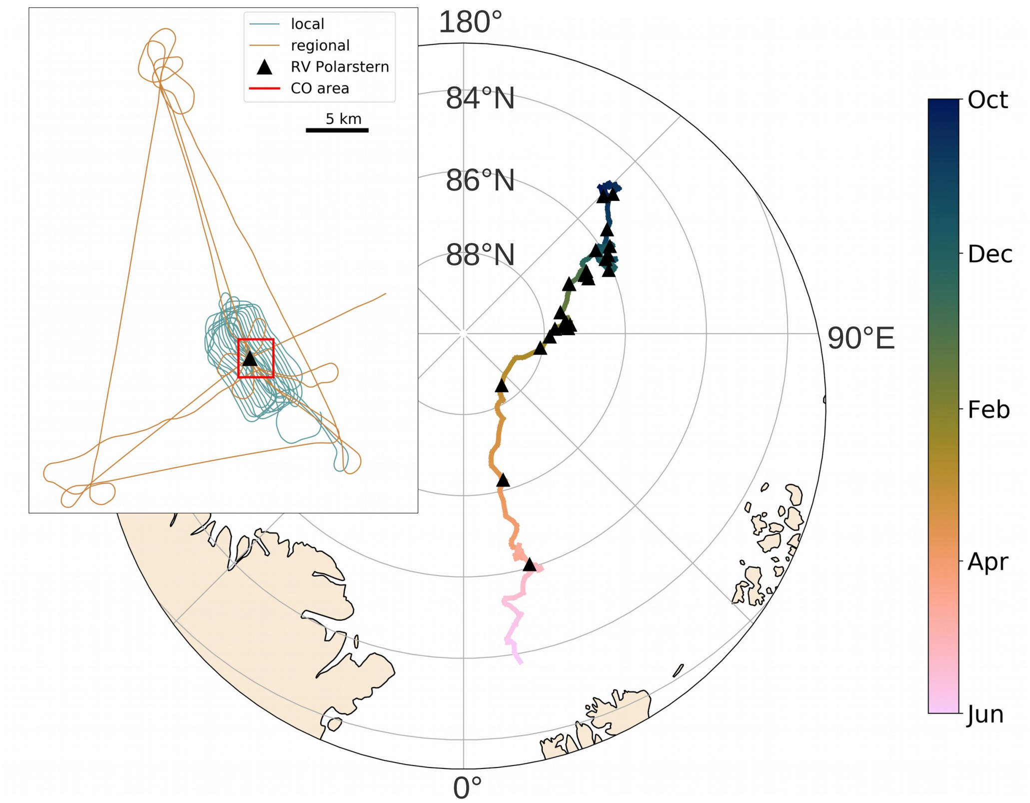

Figure 1. Helicopter flight locations and flight patterns

The colored track shows the drift of RV Polarstern from October 2019 until June 2020. The black triangles represent the location of the 35 helicopter flights. Additionally, as inlay on the left, we show a typical local (turquoise) and regional (orange) flight pattern with Polarstern as the center (black triangle). The red box marks the CO area (according to Figure S1, in Supplemental material).

to be influenced by atmospheric changes through the radiation balance at the snow/ice-air interface. Clouds strongly influence the surface temperature (Vihma and Pirazzini, 2005), i.e., they reduce the radiative cooling (Wang et al., 2001). Our flights were performed only during calm and clear weather conditions. Thus, we can neglect a dependence on changing cloud cover. However, the changing air temperature still plays a role, which needs to be taken into account (Thielke et al., 2022).

2.2. Meteorological context

How representative are our results from the MOSAiC winter in terms of surface temperature and lead area fraction in context with the meteorological condition? The meteorological conditions are discussed in Rinke et al. (2021) based on the ERA5 reanalysis data between 1979 and 2019. There were mostly typical meteorological conditions present during MOSAiC, although some unusual events happened during our observation period and before the expedition. Summer 2019, before the MOSAiC expedition started, was very warm and had unusually long low sea ice extent as well as thinner ice (Rinke et al., 2021; Krumpen et al., 2020). During the expedition, unusual conditions occurred during the following periods, all according to Rinke et al. (2021):

- Unusual cold at the beginning of November 2019 and March 2020
- Warming events in mid-November, beginning of December, mid-February, and mid-April
- Unusual positive Arctic Oscillation with associated fast sea ice drift in spring 2020 (Krumpen et al., 2021; Dethloff et al., 2022)
- Anomalous low pressure January to April 2020 associated with more frequent storm events during winter and spring (relatively low cyclone counts for October 2019 – January 2020)

2.3. Supporting data

We use atmospheric data from the 12 m meteorological mast on the MOSAiC ice floe, i.e., 2 m air temperature, measured with a Vaisala HMT 330, and 10 m wind speed, measured with a Metek uSonic-3 cage Cox et al. (2021). These supporting measurements were measured at the location of Met City in the CO (Details see Shupe et al. (2022)).

3. Surface temperature variability

This study focuses on the gridded time-fixed helicopter surface temperature maps (Thielke et al., 2022), which will be referred to as surface temperature for simplicity. Based on the series of 35 helicopter flights with the TIR camera during the MOSAiC winter, we present and discuss the spatio-temporal surface temperature variability. We present and discuss the complete seasonal cycle of the MOSAiC ice floe and its surrounding for the whole winter 2019/2020. There are unprocessed data from nine more flights available (for detailed explanation see Thielke et al. (2022)).

3.1. Temporal variability

Ice surface temperature varies even on short timescales, i.e., within the flight duration of 90 minutes. This effect, however, is largely corrected in our data set. See Thielke et al. (2022) for how the corrected and time-fixed surface temperature maps are calculated. Here, in the following, we discuss the surface temperature seasonal variability. The average surface temperature decreased from 02 October 2019 at 265.6 K until it reaches its minimum with 231.8 K on 28 January 2020 (Figure 2 A). Later in the winter season, the average surface temperature increased to 251.4 K until the latest flight on 23 April 2020, while at that time, the 2 m air temperature was already about 20 K higher and close to the freezing point. However, the temporal evolution of the surface temperature is comparable to that of the 2 m air temperature. This is consistent with our expectation that, due to the shallow penetration depth (micrometer range) of electromagnetic waves in the thermal infrared region, air temperature will have a substantial influence on our surface temperature observations. Also, Vihma and Pirazzini (2005) highlight the importance of the surface temperature and coupling to the atmosphere. At the same time, the heterogeneity of the surface temperature in ice-covered regions can also influence the atmosphere. But as long as the surface is frozen, the surface temperatures stay well below the freezing point. The surface temperature can be cooler during clear sky conditions due to radiative cooling. A prominent interruption in the cooling happened at the beginning of the winter in mid-November due to a substantial increase in the surface and air temperature caused by a storm event (Rinke et al., 2021). More warming events (subsection 2.2) are reflected in the surface temperature record. From mid-February onward, the frequency of flights was reduced, so we cannot reflect all single atmospheric events. However, we can show the warming of the surface temperature towards spring.

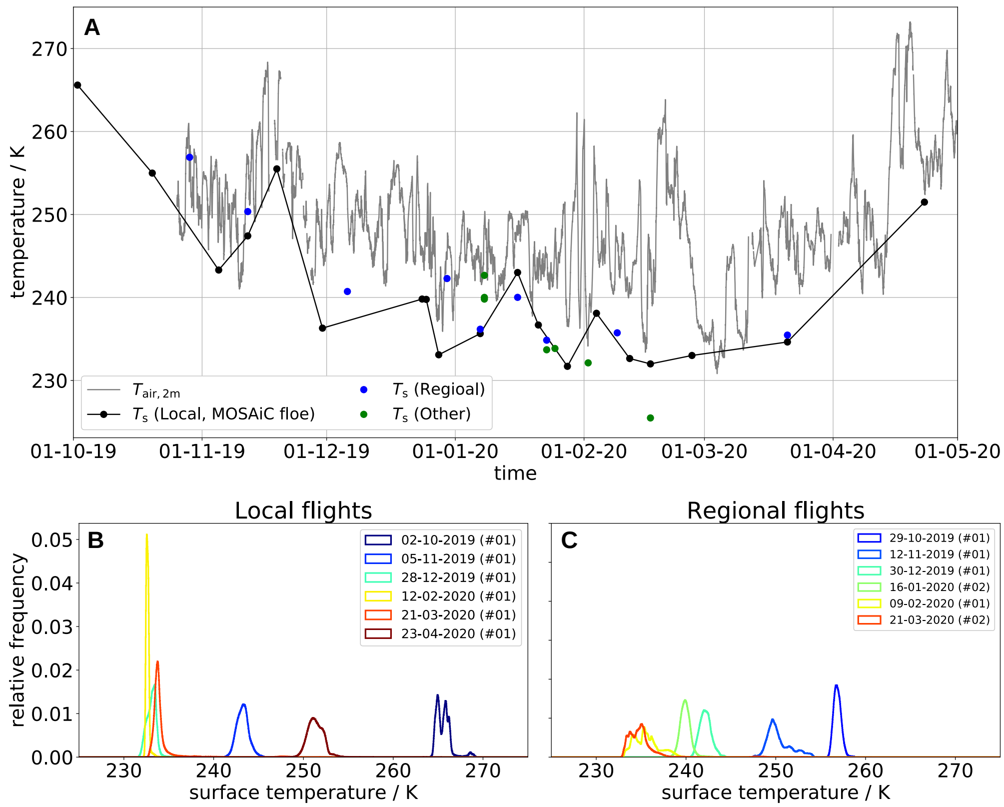

Figure 2. Evolution of MOSAiC surface temperatures from 35 helicopter flights.

(A) Temporal evolution of the average surface temperature throughout winter 2019/2020 from 02 October 2019 to 23 April 2020. Black indicates the local flights covering the Central Observatory (CO). They are connected to show the temporal evolution of the primary MOSAiC observation area. The regional flights, repeatedly visiting the L-Sites in the MOSAiC distributed network, are displayed in blue, whereas green shows additional flights not falling in one of these two categories. The grey line represents the 2 m air temperature measured at the floe in Met City. In the lower panel, a selection of surface temperature distributions is shown for different dates in the winter for (B) the local and (C) the regional flights. The colors continue from blue (begin of the winter) to red (end of the winter).

3.2. Spatial variability

In January 2020, there is a high density of flights, which allows us to illustrate the variability between different scales nicely or even on a short timescale for similar spatial surveys (Figure 2 A). On 07 and 16 January 2020, a local (black) and a regional (blue) flight were conducted on the same day (the regional flight is in both cases about 3 hours later). On 07 January, the average surface temperature of the different flights is similar, with an increase of only 0.6 K for the regional flight, which corresponds to an increase of 0.8 K in the 2 m air temperature. On 16 January 2020, the difference is larger with a decrease of 2.7 K while the 2 m air temperature only decreased by about 0.9 K. Thus, changes in the spatial surface temperature variability, either on the local or regional scale, has to explain the increasing temperature difference within nine days between the local and regional scale (flights had similar flight patterns). A likely candidate would have been changing lead fraction but actually a change of number of leads does not seem to be the reason for the higher temperature difference on 16 January: On 07 January there is actually a higher lead area fraction for the colder local flight (2.02% vs. 0.23% for the regional flight, see Table 1). While on 16 January 2020 the colder regional flight had a higher lead area fraction (1.37% vs. 0% on local scale; see Table 1). Thus, likely changes in other ice types with different thermal properties, snowfall, or snow redistribution should have caused these changes in spatial surface temperature variability.

The spread of the surface temperature varies from flight to flight. It is illustrated with the exemplary selection of six surface temperature distributions for local and regional scales throughout the winter season (Figure 2 B, C). Mostly, the distributions are wider for regional flights (right) than for local flights (left) because they include a larger variety of surface types due to the wider spatial extent. The major peak represents the predominant surface type, snow-covered thick ice, in all cases. The surface temperatures of this thick ice are more similar to the 2 m air temperature because of the reduced heat flux from the ocean through the thick ice and snow (Shokr and Sinha, 2015). The warm tail shows the presence of leads, but its peak is often too small (only visible in the log-scale), and the different thin ice thicknesses in leads of different ages widen the lead temperature distribution. In the local flights, we can find a transition from a wider distribution at the beginning of the winter season (blue) to a narrow distribution in mid-winter (yellow), and back to a wider distribution towards the end of the winter season (red). The more narrow distributions indicate the prevalence of the thick, consolidated ice due to cold and constant conditions. A wider distribution indicates the presence of several ice classes and spread towards warmer temperatures.

In the time series, we could already show the close connection to the atmospheric state, represented by the 2 m air temperature. Additionally, we look at the dependence of the surface temperature standard deviation, as a measure of spatial variability, (leads were excluded to have a comparable basis of the thick ice) on the 10 m wind speed (Figure S2, in Supplemental material) . We expect a lower surface temperature standard deviation for higher wind speeds caused by an increased exchange between the surface and atmosphere. We find a correlation of –0.38 between the surface temperature standard deviation and 10 m wind speed around the target time of the flight with the significance of a p-value of 0.04. The relationship with wind speed supports our assumptions that increasing wind speeds reduce surface temperature variability and can explain the greater sensible heat exchange due to faster air mass exchange. Because leads are not taken into account here, a potentially more dynamic ice pack that would result in more leads (and thus greater temperatures) can be ruled out. There is no relation between the average surface temperatures and the standard deviation. Although a low-temperature regime can create more compact and consolidated ice (uniform temperature), even under cold conditions, deformation can cause variability in ice classes with warmer surface temperatures, which increases the variation.

4. Lead classification

The leads are classified based on a one-dimensional, temperature-only approach, i.e., leads are characterized by a specific surface temperature range, defined by the temperature distribution of the corresponding flight. We apply a binary classification, discriminating between sea ice (snow-covered thicker ice) and leads, which are mostly covered with thin ice due to the fast freezing of the ocean surface under cold winter conditions. The classification is applied to the surface temperature grids. The pre-processing described in Thielke et al. (2022) avoids the influence of changes in surface temperature during one flight. The thermal distinction for surface types with larger ice thickness is getting weaker due to low heat transfer through the ice (Maykut, 1978). Thus, the discrimination of leads from thick ice is easier due to large temperature differences, and we do not aim to discriminate the thick ice classes further (e.g., in first-year and second-year ice). We apply dynamic thresholds for different flights (Table S1, in Supplemental material and subsection 4.1) in order to establish the same classes defined with different surface temperature distributions in different flights.

The dynamic threshold is required because the surface temperature is strongly connected to the ambient air temperature, which is strongly variable with time (see subsection 3.1).

4.1. Iterative threshold selection

We apply the iterative threshold selection from Ridler et al. (1978) to the two-dimensional temperature arrays. The temperature distribution has its major mode towards the colder part of the distribution and a smaller secondary mode along the tail towards the warmest temperatures (caused, e.g., by leads). The initial threshold is the middle range of the temperature distribution (average of the minimum and maximum value). Due to the long tail towards the warmer temperatures, it is ensured that the initial threshold is on the warmer side of the major mode so that the iteration can converge towards a minimum between the two modes Starting from the initial threshold, the threshold is adjusted iteratively based on the new ”lead” mask (defined by the threshold of each iteration) for the temperature array until it reaches the final temperature threshold. The updated threshold is calculated from the mean of the ”lead” (all values larger than the threshold) and ”sea ice” (all values smaller than the threshold) temperatures based on the current threshold. The iteration stop criterion is achieved when the temperature threshold change between one iteration to the next is within the tolerance of 0.02 K, which corresponds to the precision of the IR camera. The main steps are shown in the flowchart in Figure 3, and the Python3 code is shared in part A of the Supplemental material. For three flights (20191224_01, 20191225_01, 20200108_01), the threshold did not converge to a reasonable value; therefore, the tolerance had to be increased to 0.8 K. For the cases with this larger allowed tolerance in the difference, the obtained threshold still results in a reasonable lead classification, i.e., can be confirmed by the manual classification (see below in subsection 4.2).

4.1.1. Classification example 20 October 2019

The threshold-based lead classification is shown for the flight on 20 October 2019 at the beginning of the winter season in Figure 4. We show steps 0 (initial threshold) to 2 for the temperature threshold iteration (A). With step 2, the result is already close to the final result (step 5) shown in (D). The surface temperature (B) is dominated by low temperatures (blue), associated with snow-covered thick ice. The warm surface temperatures (red domain) are referred to as leads. The binary classification map (D) resulting in ”sea ice” (gray) or ”leads” (red) is based

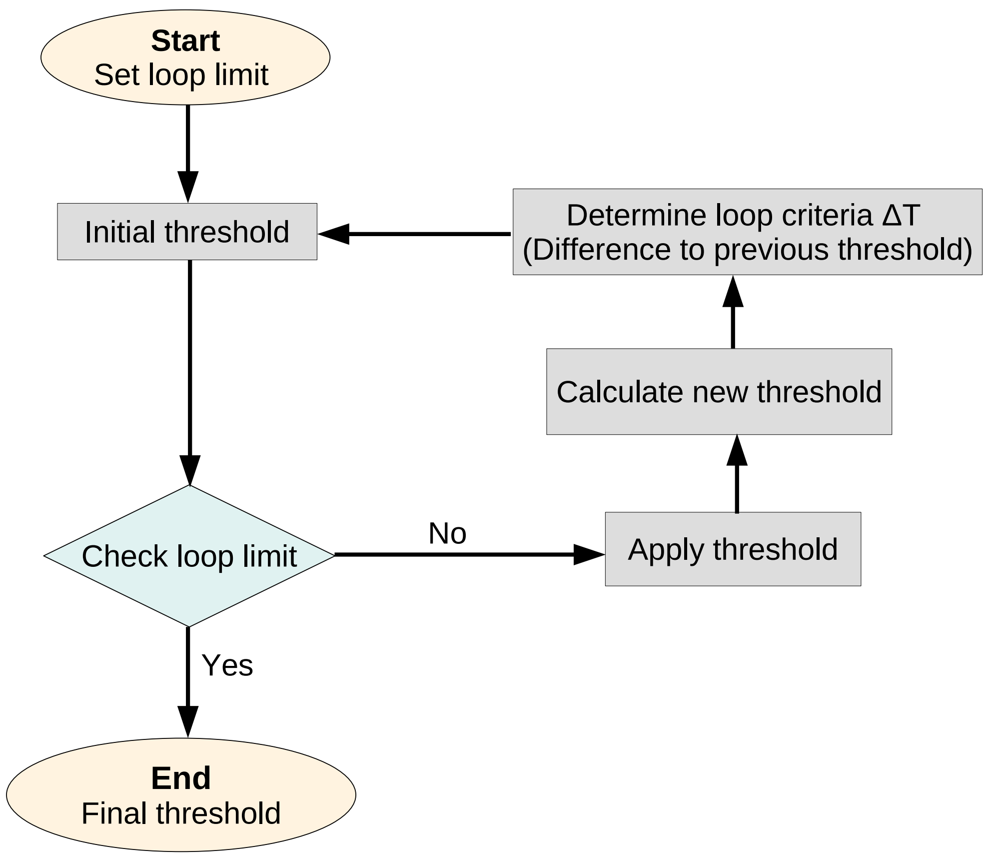

Figure 3. Flowchart for the processes of the iterative threshold selection.

Main processing steps for the iterative threshold selection to determine a temperature threshold for lead classification.

on the iterative temperature threshold applied to the temperature distribution (C), showing the two classes as two main temperature regimes. The lead area fraction for this case on 20 October 2019 is the highest in our time series, with close to 10% for the full area covered by the helicopter flight.

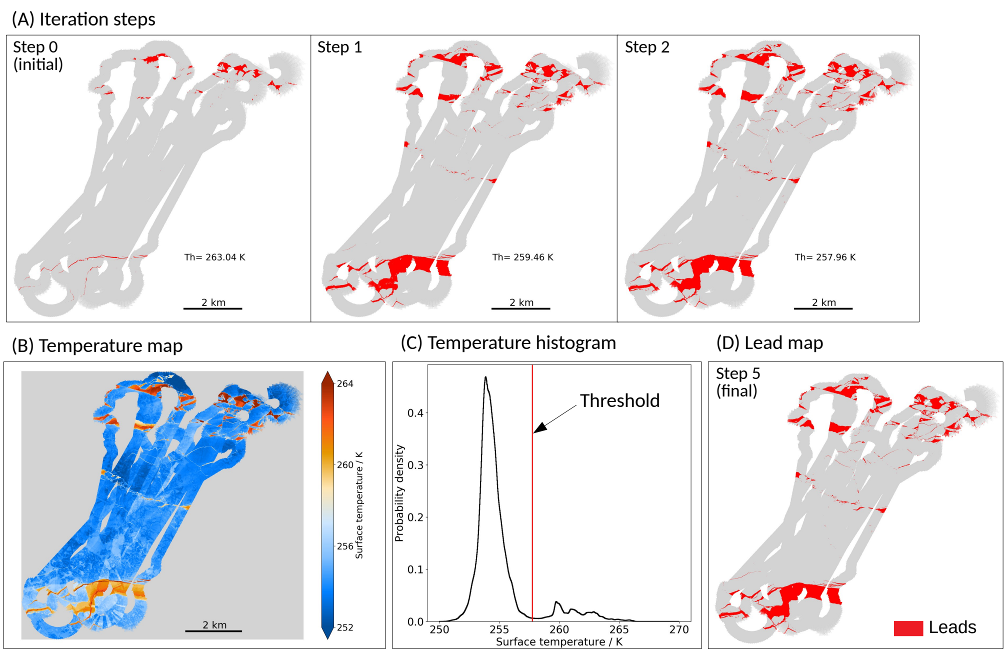

Figure 4. Lead classification example for the flight on 20 October 2019.

(A) Results from steps 0, 1, and 2 for the iterative threshold selection. (D) Final (step 5) binary lead classification based on (B) the gridded surface temperature maps. (C) The temperature distribution of (B). The red vertical line represents the found iterative temperature threshold to discriminate between "lead" and "no lead" surfaces.

4.2. Evaluation using manual thresholds

We use manual thresholds as a comparison for the reliability of the iterative method. The authors performed the manual threshold selection based on the minima in the distribution and visual approval of the classified map compared to the surface temperature map. The manual selection is a rather arbitrary and conservative choice but it can be used for the evaluation of the automatic, iterative classification method. The thresholds are determined for each flight individually because the surface temperature values and their distributions change from flight to flight. The manual selection was, in some cases, more conservative, i.e., it has warmer thresholds but does not significantly influence the resulting lead area fractions (Table S1, in Supplementary material). Although the manual temperature threshold is 1.97 K higher than the one from the automatic and reproducible method (subsection 4.1), its derived lead area fraction is only 0.1% lower than for the iterative method. Thus, the threshold difference does not significantly affect the lead area fraction because it is in the minimum of the surface temperature distribution. The small difference demonstrates that the automatic method aligns well with the manually defined thresholds and the resulting lead classification. We chose results from the automatic method for the following discussion because it is reproducible and can also be applied to further flights.

5. Winter lead area fraction

5.1. Lead formation during the November storm event

Here, we discuss the storm event, which happened from 16 to 20 November 2019 (Rinke et al., 2021). This event had a major influence on the MOSAiC Central Observatory (CO) due to several leads appearing across the measurement sites. It had a significant relevance for several measurements (Nicolaus et al., 2022; Shupe et al., 2022) and was, e.g., influencing the snow transport as discussed in Nandan et al. (2022). We conducted one flight before (12 November 2019) and one flight after the storm (19 November 2019) and compare both flights directly in Figure 5. This storm event with high wind speeds was associated with warm air advection. It resulted in increased ice dynamics, which caused the break-up of the sea ice along various fracture lines, which are visible in Figure 5 B and D. The surface temperatures on 19 November 2019 after the storm are overall higher than before the storm event (mind the different temperature scales for (A)/(C) and (B)/(D)). Before the storm, there are a few narrow cracks in the outer areas of the flight pattern (Figure 5 (A)), but no prominent cracks in the vicinity of RV Polarstern (Figure 5 (C)). The surface temperature map of 19 November 2019 includes warm linear structures throughout the CO area and beyond (Figure 5 (B, D)), which causes an increase of lead area fraction from 0.07% (Figure 5 (C)) to 1.73% (Figure 5 (D)) and therewith to a higher surface temperature variability.

5.2. Spatio-temporal variability

We discuss the spatio-temporal variability of the lead area fraction, which was calculated based on our lead classification (section 4). The local lead area fraction

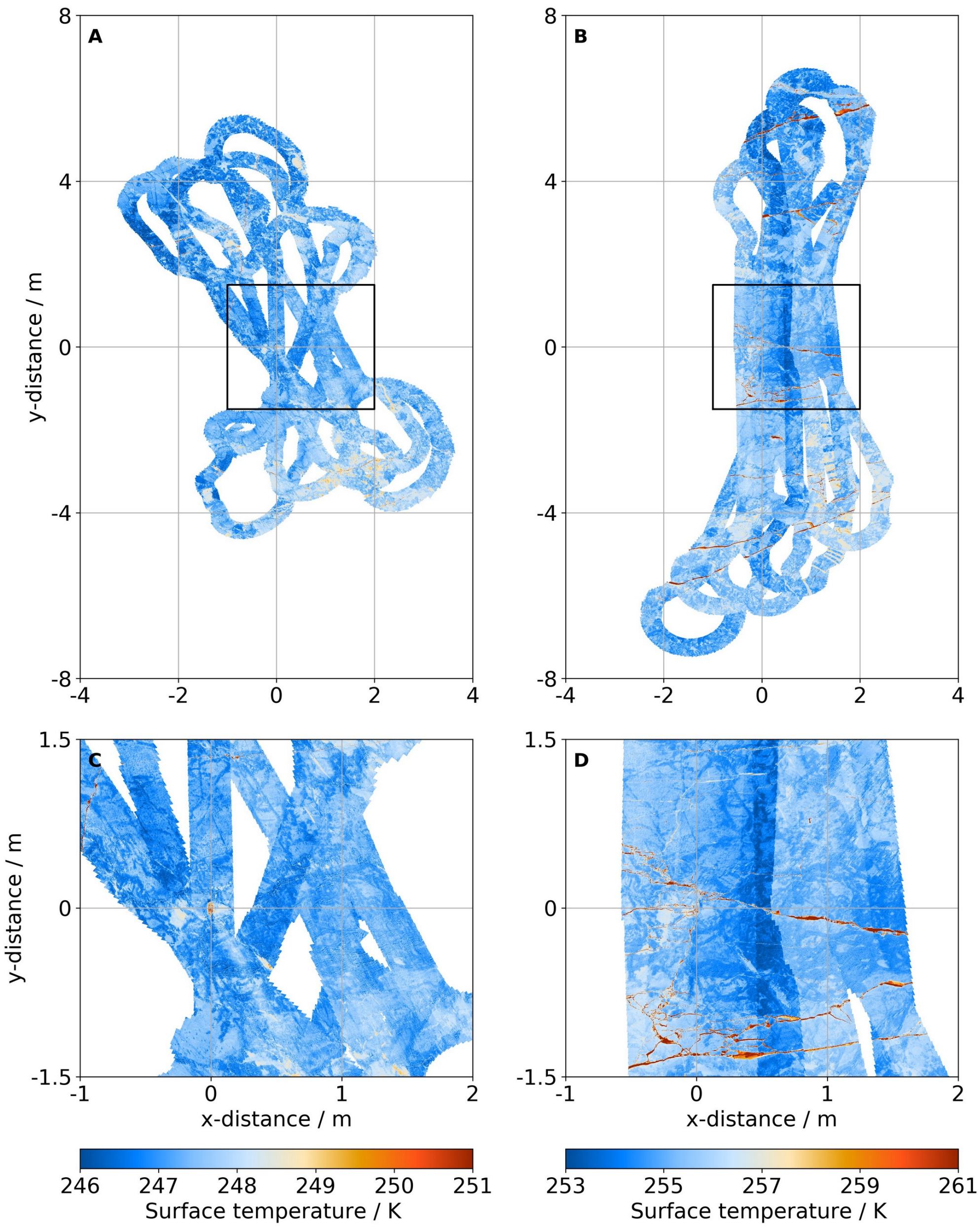

Figure 5. Surface temperature maps before and after the November storm event.

Comparison of two time-fixed surface temperature maps displayed in relative coordinates before the storm event (A, C) on 12 November 2019, and after the storm event (B, D) on 19 November 2019 with their respective CO area around RV Polarstern (0,0). Please note the different temperature ranges, adjusted to allow clearer visibility of the spatial variability of the temperature. For the flight on 19 November 2019, an increased area of warmer temperatures (reddish) is prominent.

(orange line in Figure 6) is constrained to the CO area of 3×3 km. In the CO area (shown in Figure S1 in Supplemental material), always the same area around RV Polarstern is covered and makes the lead area fraction better comparable during the winter season as for the entire local flights. In most cases, the CO area lead area fraction is close to the one for the complete local flights (not shown); however, there is a large difference in lead area fraction on 20 October 2019 (1.3% for the CO area; 10.2% for the full local flight) because the majority of the detected leads are outside of the CO area. The data coverage of the CO area is sufficient for all flights with more than 50% and, except for the flights in November, even with more than 75% (Figure S3, in Supplemental material). The lead area fraction within the CO area shows high variability between 0% and 4%, but no trend can be seen in the temporal evolution (Figure 6, orange line). For the November storm event (subsection 5.1), there is an increase in lead area fraction for the CO area from close to 0% on 12 November 2019 to 1.7% on 19 November 2019. We find for the regional scale, there is a steady low lead area fraction between 0% and 1% until mid-January. Towards the end of the winter season (21 March 2020), the lead area fraction increases to up to 4%. The increase in lead area fraction might be related to the increased number of storm events between January and April, compared to previous months (subsection 2.2).

The higher lead area fraction observed in March in our data aligns with the temporal lead area evolution discussed for the regional scale in Krumpen et al. (2021). However, they observe a distinct higher lead area fraction of up to 20%, derived from MODIS TIR satellite data. The regional lead area fraction evolution also agrees well with the regional Satellite Synthetic Aperture Radar (SAR) derived time series from Guo et al. (2022), which is in the similar range of 0-4% as ours and starts to increase only in March. Kortum et al. (2022) performed an ice classification based on SAR satellite data during winter on the same scale as our CO area. Our leads should be represented by the sum of open water and young ice classes of this study, where daily data are available (higher temporal resolution than our data). Their daily data generally show a comparable to our lead area fraction below 5% in mid-winter but exceed this value on a few days to up to 15% around 23 November 2019. Additionally, during March and April, their lead area fraction is for a longer time on a higher level of up to 10%. The high values at the beginning of the winter in Kortum et al. (2022) might be caused by the characteristics of the method based on SAR data. The same method from Kortum et al. (2022) was applied on the regional scale. The regional lead area fraction has a peak in mid-November of 6%, stays below 4% and even lower during mid-winter, and increases in the second half of March to 7% (Karl Kortum, personal communication on 08 December 2022). While we do not capture their peak in November and the absolute values differ with a few percentage points, also the regional evolution aligns with our time series. Thus our results align reasonably well (considering different temporal and spatial sampling) with the two SAR-based studies, while for the MODIS TIR based study only the temporal evolution agrees but the absolute values are different (much higher in the MODIS lead time series).

Within our data, we see scale-dependent differences in the lead area fraction with less variability on the regional scale than on the local CO scale but no trend in the local scale, while the regional lead area fraction increases throughout the winter (Figure 6). Nevertheless, the overall magnitude is similar. Thus the CO area is representative of the measurement sites in the CO of the MOSAiC expedition but the temporal development does not necessarily represent the lead area fraction on a larger scale. Nonetheless, the local data are helpful for a better understanding of the condition at and around the MOSAiC floe, particularly in connection to other in-situ measurements. Our lead area fractions (0-4%) are comparable to other previous studies of Marcq and Weiss (2012) with 1–2%, and Lindsay and Rothrock (1995) with 2–3%; both these winter lead area fractions were also derived in the central Arctic. Generally, the lead area fraction for the MOSAiC winter seems to align with the climatological mean and might be influenced by the changing location due to the MOSAiC drift (Krumpen et al., 2021). Yet, comparing different lead area fraction retrievals remains challenging because of different definitions of leads (e.g. open leads vs. leads covered by thin ice or even frost flowers) with other methods used on different scales (von Albedyll et al., 2022).

5.2.1. Relation to wind speed

We are interested in the connection between lead area fraction and wind speed because wind events can cause increased ice dynamics and, therefore, possibly more leads. Thus, we compare our lead area fraction to the 10 m wind speed. We use the 7-day running mean for the wind speed to find prominent high wind regimes rather than short-term fluctuations because we can not represent these fluctuations with the limited temporal frequency of the helicopter flights.

We do not find significant correlation between wind speed and lead area fraction on the local and regional scale. However, we see sometimes a relation, such as for the increase of the lead area fraction (Figure 6) during the November storm event (subsection 5.1). We have to note that our flights are only snapshots of a specific time with a weekly to biweekly frequency, while leads can open and close within hours. However, in most cases, they prevail for several days (if not closed by another ice dynamic event) until, eventually, the ice thickness and snow accumulation within them gets too thick to be discernible from the surrounding ice in TIR imagery.

We highlight two cases in our time series: 1) the highest local lead area fraction within the CO area of 4% end of December occurs after a high wind regime that lasted several days, and 2) basically no presence of leads in mid-January during an increased wind speed regime while the regional fraction increases. Especially the high lead area fraction variability for the local CO area illustrates that local changes are rather random, not always representing large scale changes (see different temporal development between local and regional lead area fraction). Nevertheless, the local lead area fraction is valuable in combination with other interdisciplinary measurements obtained during MOSAiC and valuable for getting a better process understanding.

6. Lead properties

6.1. Lead segmentation

We apply a segmentation algorithm to the lead map to define the properties of single leads, i.e, width and orientation. The segmentation is performed according to the watershed segmentation (Najman and Schmitt, 1994). Next, a set of object lead properties (width and orientation from enclosing ellipse, its area, orientation, and major axis) is derived based on (Burger and Burge, 2009) with 'scikit-image' library for Python.

In Figure 7, we illustrate the object properties for two example lead segments. The warmer temperatures on the left (yellow) are classified as lead, consistent with the red areas on the right that indicate the lead areas. We retrieve the lead properties width and orientation (calculated from ellipse parameters), assuming the lead properties are representative, even if the ellipse does not cover the full lead due to the limited spatial coverage of our data or if the lead is interrupted. We therefore can only determine width but not length of the leads. The key lead parameters are the classified area (red) in the enclosing rectangle (dashed line in Figure 7), minor and major axis, as well as the orientation of the ellipse (pointing in the direction of the major axis). The zero line for the orientation is the north-south axis (all our surface temperature maps are oriented North along the y-axis). The ellipse defined for the lead segment is not representing the real length, but can be seen as a stable approximation for an object of arbitrary shape. Generally, the ellipses of close-by leads can overlap, which is required

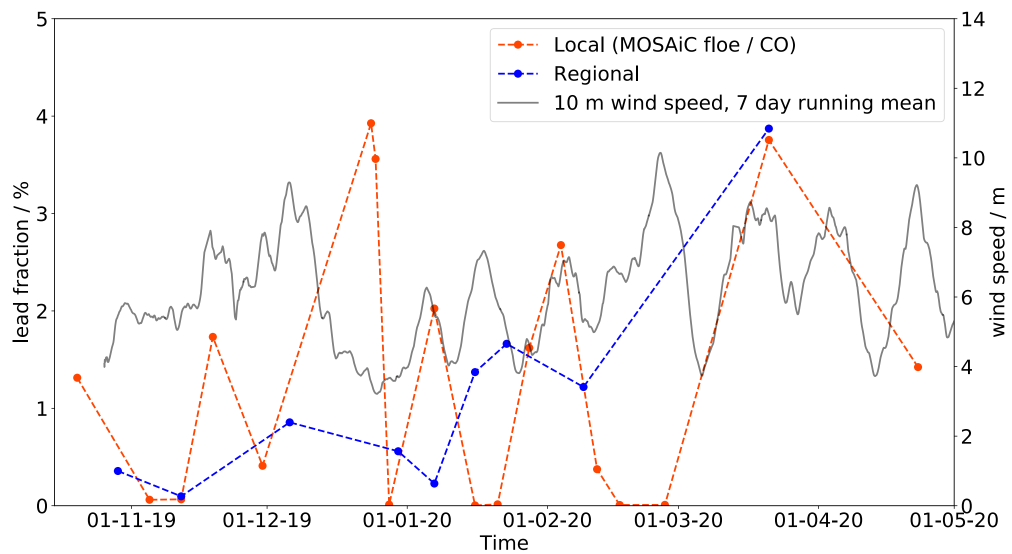

Figure 6. Evolution of the lead area fraction on different scales.

Temporal evolution of the lead area fraction throughout winter 2019/2020 from 02 October 2019 to 23 April 2020. The orange points show the lead area fraction for the CO area. The blue points illustrate the lead area fraction for the regional flights, visiting the L-Sites. The grey line shows the 10 m wind speed averaged to a 7-day running mean. Please note that there might be a minor influence by in and out coming support vessels, which could slightly increase the lead area fraction by breaking the ice.

Table 1. Lead area fraction values from Figure 6.

Lead area fraction values for the local and regional scale in %. The same as the displayed values of the data shown in Figure 6.

Date	Local fraction / %	Regional fraction / %
2019-10-20	1.31	-
2019-10-29	-	0.36
2019-11-05	0.06	-
2019-11-12	0.07	0.10
2019-11-19	1.73	-
2019-11-30	0.41	-
2019-12-06	-	0.86
2019-12-24	3.93	-
2019-12-25	3.56	-
2019-12-28	0.01	-
2019-12-30	-	0.56
2020-01-07	2.02	0.23
2020-01-16	0.00	1.37
2020-01-21	0.01	-
2020-01-23	-	1.66
2020-01-28	1.62	-
2020-02-04	2.68	-
2020-02-09	-	1.22
2020-02-12	0.37	-
2020-02-17	0.01	-
2020-02-27	0.01	-
2020-03-21	3.76	3.87
2020-04-23	1.42	-

to calculate the lead properties individually, even though the two lead segments are not overlapping (Figure S4, in Supplemental material). We must deal with some artificial effects, such as the map's edge or shifts inside the map caused by small offsets in the geolocation of different helicopter overflights. Shifts or gaps could cause an artificial break of a lead into more segments, whereas it would have been only a single lead. Also, due to ice drift direction changes (i.e., shear), which can cause real breaks and gaps in the classified leads, the segments can represent a subset of a lead. The segments of the subsets of leads will result in an overestimation of the total number of leads. However, it is not expected to impact our results for lead width and orientation (we do not analyse the number of leads). Therefore, we assume that the segmentation is representative of our purpose of an overall statistical analysis of lead width and orientation. Width and orientation may also be critical parameters for evaluating the turbulent heat flux from leads (Tschudi et al., 2002). On the one hand, the efficiency of the heat transfer is dependent on the orientation relative to the wind direction (e.g., Tetzlaff et al., 2015). On the other hand, the heat transfer is more efficient for narrow leads, which makes the transfer dependent on the lead width distribution (Marcq and Weiss, 2012).

6.2. *Lead orientations*

A good understanding of lead orientation is crucial because they represent the ice dynamics of the sea ice (Lindsay and Rothrock, 1995). Ringeisen et al. (2019) emphasize the lack of knowledge of lead orientation at the floe scale because of missing high resolution observations. Here, the MOSAiC observations like ours can contribute new data. Better knowledge of small scale leads is also crucial for a good representation of ice rheology in sea ice models (Hutter et al., 2018; Ringeisen et al., 2021). The orientation of leads shows the effect of ice dynamics in sea ice, influences it, and is connected to prevailing regional wind and ocean current (Lindsay and Rothrock, 1995). In the long term, leads have a non-random orientation during the Arctic winter, mainly influenced by coastlines and atmospheric and oceanic currents (e.g., Bröhan and Kaleschke, 2014). In general, lead features, including width and orientation, are similar across a large range of scales, including the smallest scales (Schulson, 2004).

We here look at the lead orientations of nine local flights (full coverage, i.e. not restricted to the CO area), which have in the CO area a lead area fraction of $\geq 1\%$. This ensures a sufficient presence of leads to perform a statistical analysis of lead orientations. We decided not to connect the single lead segments which might be

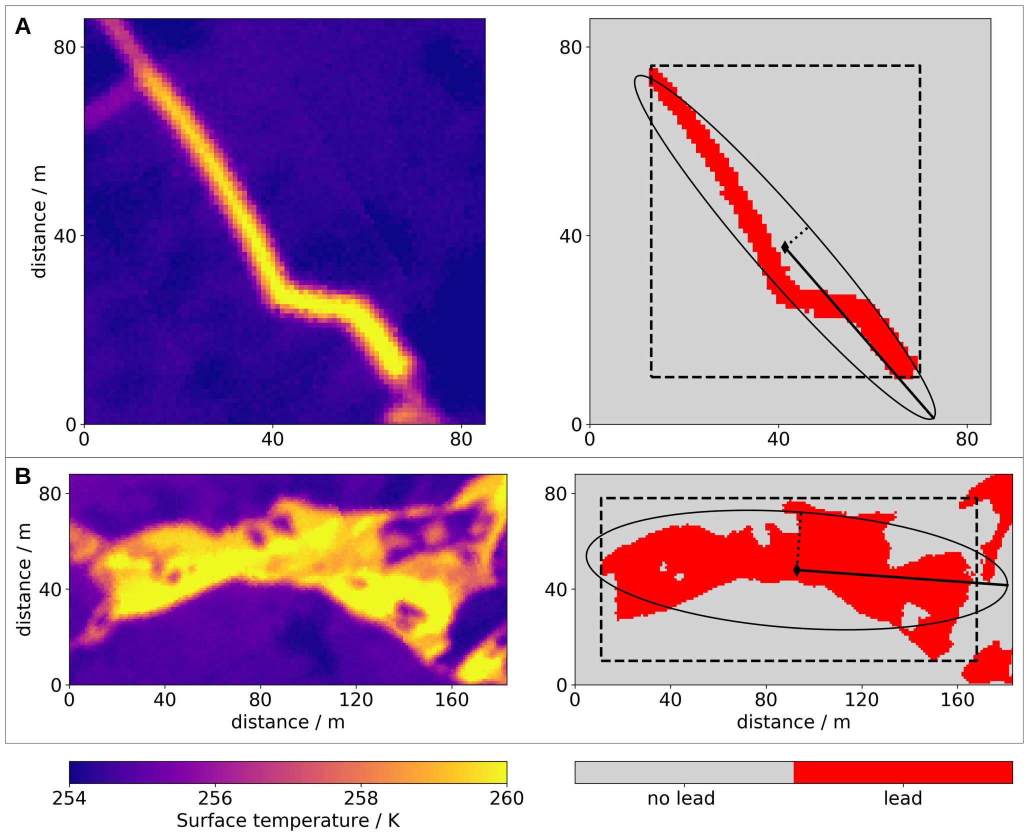

Figure 7. Lead segmentation to derive lead width and orientation properties.

Two lead segments from the lead classification result of the flight on 20 October 2019 with the temperature map on the left and the lead classification including the ellipse geometry on the right. The ellipse and their major axis (solid) and minor axis (dotted) are shown. The dashed rectangle marks the area from which the classified area in red is determined. (A) Shows a narrow lead with a mean lead width of 3 m and an orientation (of the major axis) of –41°. (B) Shows a wider and slightly scattered lead. It has a 26 m mean width and –86°as orientation.

split within one lead (subsection 6.1) because we look at statistical distributions of lead properties and do not distinguish single leads. Furthermore, we bin our data in 5° steps.

Comparing the nine flights between 20 October 2019 and 23 April 2020, we see a high temporal variability in the lead orientation distribution (see examples in Figure 8), also shown for passive microwave based analysis in Bröhan and Kaleschke (2014). We find prevailing orientations of –80°, –10°, 30°, or 60° (Table S2, in Supplemental material). In the following part, we focus on three examples from 07 January 2020, 28 January 2020, and 21 March 2020 (Figure 8). We identify modes of the lead orientation probability distributions of the orientation from –90 to 90°, binned in 5° steps (Figure S6, in Supplemental material). We constrain our data to elongated ellipse shapes with an axis ratio (major/minor) of at least two. Additionally, we compare the leads of all widths with leads of a width of more than 3 m which is consistent with the valid range of the power law. With the constraint of the axis ratio, the data are reduced to 89% of the full data set. With the minimum width of 3 m the data amount is reduced to 21% of the complete data set. Starting with the case in March (Figure 8 C), we cannot find a major peak in the distribution of all lead width. With only wider leads ($\geq$ 3 m), the distribution of orientation angles is modified to a preferred direction at 35°, but still most orientations are present and not a clear prevailing orientation can be identified. Going backward in time to the end of January (Figure 8 B), we have one prominent orientation at –35° (all leads) which is even more emphasised for leads with the minimum width of 3 m (slightly shifted to –30°). There is a second minor peak at 40°, but this is very small and does not allow us to infer any intersections between two main orientations. For the case on 07 January 2020 (Figure 8 A) we identify one clear main direction of –10°. We see a variation in the primary lead orientation throughout the winter but no prevailing orientations on longer time scales. For none of the nine investigated flight we can infer two main directions (bimodal distribution) from which we could infer an average intersection angle. Usual lead intersection angles from different studies, including satellite and laboratory measurements, would be 30–50° (Hutter et al., 2022), also shown for a SAR data set from MOSAiC Ringeisen et al. (2022). There is a difference between using all data and the width restricted subset, but overall both show the same picture (Table S2, in Supplemental material). The variability might depend on the regional wind patterns that create direction-related fracture patterns. The investigation of the reasons for the variability in lead orientation is beyond the scope of this study, but is encouraged for future research. Different to many previous studies is that we are (a) far from land (which can introduce prevailing lead orientation by restricting ice drift in one direction) and (b) following the Lagrangian approach of the MOSAiC drift, which results in different locations of the Arctic Ocean to be monitored.

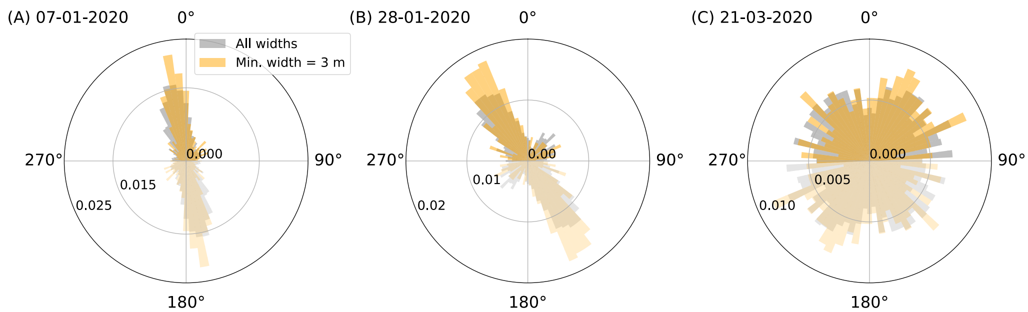

Figure 8. Orientation angles of leads for three example cases.

Probability density distribution for the orientation angles of the flight from (A) 07 January 2020, (B) 28 January 2020, and (C) 21 March 2020, as polar histogram. The radius indicated the probability density, which is different for all three cases. Only lead segments with an axis ratio (major/minor) ≥ 2 are included. We discriminate between two cases: leads of all widths included (gray) and only leads with a minimum width of 3 m included (orange). The lead orientation have only a range of 180°but are valid in both directions, they are mirrored to the opposite direction (slightly transparent). The total number of lead segments used for the histograms (270°to 90°only) are (all; $\geq$ 3 m): A=(1736; 500), B=(1326; 303); C=(1378; 464).

6.3. Lead width distribution

We discuss here the power law scaling of lead width (i.e. many more narrow leads than wide leads). Equation 1 gives the relation between lead width and number of observed leads (as probability density) of a respective width assuming a power law relationship:

$$f(x) = ax^{-b}. \tag{1}$$

The parameter a is the scaling parameter (related to the number of measurements), but not further analysed here. The parameter x is the variable lead width, and b is the power law exponent, determining the (negative) slope. Thus, a larger power law exponent b results in a steeper (more negative) power law. The ratio of the classified segment area (shown in red in Figure 7) and the major axis length of the ellipse approximates the lead width. We detected in total 33855 lead segments in our classified maps for all 35 flights (but see explanation above why the number of segments should not be mistaken as the number of leads). The detected lead width varies between 1 m and 464 m. From the distribution of the lead widths, we perform a linear fit for Equation 1 (Figure 9 A) in the log-log space with logarithmic bins. We exclude leads smaller than 3 m width because they are too close to the spatial resolution of the data set to be fully resolved in the segmentation. This can be seen from the deviation from the power law below 3 m in Figure 9. This is confirmed by the stabilisation of the power law exponent for a minimum lead width of 3 m and larger (Figure S5, in Supplemental material). However, for a minimum lead width between 9 m and 26 m we see an slight increase of the power law exponent. We do not know the reason for the increase but our hypothesis is that the value is less reliable because of the strong decrease of number of observations available for the power law fit. Our power law is calculated up to the lead width of 336 m (largest logarithmic bin). The resulting exponent of b=2.63 agrees with literature values at the upper end of the previously found exponent value range (2.0 to 2.6) (Wadhams, 1981; Wadhams et al., 1985; Marcq and Weiss, 2012; Wernecke and Kaleschke, 2015; Qu et al., 2019) and proves the compatibility with other datasets. From the stability of b in Figure S5 (in Supplemental material) we estimate the uncertainty of our b to be smaller than the range of the literature values of 2.0–2.6. The so far presented literature values of the power law exponents are summarized in Muchow et al. (2021). Lindsay and Rothrock (1995) determines a smaller exponent of 1.6 ± 0.18 (less steep), which might differ because the power law is calculated to the lead width that is equal to the spatial resolution, while we see in our data that the power law is not valid anymore close to the spatial resolution and the slope between the bins has a smaller absolute value. In previous studies, the range of the power law exponent (dependent on the instrument and resolution) was determined starting between 20 m and 2 km lead width. Our study adds to the lower end of lead width with a range down to 3 m lead width and shows that the power law agrees with other methods and resolutions. As expressed by the power law, there are many more leads with small lead width, which were not resolved in previous studies. Also, our 3 m, the smallest resolvable lead width, likely is not the end of the lead width distribution. There are likely many cracks with a smaller width, which we do not resolve (but also can be important for, e.g., heat flux estimates). Our exponent is one of the largest (i.e., most negative) compared to the literature values. The other studies are also based on primarily winter data (Oct-Apr) but performed in different regions of the Arctic, which might influence the results due to different characteristics of the ice rheology. The power law distribution tells us that there are many more narrow leads than wider leads, which emphasizes the importance of small-scale features. The area contribution of the smallest leads are: (i) 4%, for lead width <3 m, (ii) 64%, for lead width between 3 and 100 m, and (iii) 32%, for lead width >100 m.

Additionally, we found a seasonal dependence of the power law exponent, with a tendency of an increasing power law exponent throughout the winter season (Figure 9 B). The seasonal increase in the power law exponent can also have a spatial component because of the drift into different regions during MOSAiC (Figure 1). The power law exponent drops from 2.42 to 2.14 at the start of the winter season in October (freeze-up time and consolidations of the ice north of the Laptev Sea). This is followed by a steady increase to 2.63 on 07 January 2020 (Central Arctic). Following that, there is a further increase and then stabilisation around 2.74 in March and April (North of Svalbard). Mind that we are not covering the full melting and summer season, which again might introduce a change in the exponent. For the power law exponent, there is: (i) no scale dependence (no variation between local and regional flight, also on the same day; compare black and blue dots), and (ii) no clear effect on the exponent by a rapid change in lead area fraction (subsection 5.2) caused by ,e.g., the November storm event (Figure 9 B). An increasing exponent during winter time contrasts with the findings of Lindsay and Rothrock (1995) where the monthly average of the power law exponent for the central Arctic decreases from February to April and again decrease from October to December in the following season. We can only comment on several theories without providing a certain explanation why the power law exponent increases (relatively more narrow leads) throughout the winter. Three exponents in October and the beginning of November are lower (2.1 to 2.3), probably because during the freeze-up phase the ice floes were still in rather free drift, which could more easily cause relatively wider leads (decrease of the exponent). The power law fit aligns for these three flights not as good as for the other flights, which is more prominent for smaller lead widths. In December and January, the exponent is increasing from 2.5 to 2.7, which may be related to a more consolidated and thicker ice pack far away from the coastlines (potential change of internal ice strength). This time was also characterized by less storms and lower wind speeds (Figure 6). The stabilization at the end of the winter could show the maximum power law exponent that can be reached during winter before it decreases towards the melt season with free drift conditions (which is not included in our dataset anymore).

The clear power law relationship for the lead width found here supports the validity of our lead property data and that representative statistical conclusions can be obtained from it. Our results indicate that we miss many leads in satellite remote sensing products with coarser spatial resolutions. This could already be extrapolated from the found power-law in previous studies, but is here shown for the first time down to a lead width of 3 m. Our widest leads are still narrower than the resolution of about 1 km of thermal infrared satellites. Lead retrieval results vary (e.g., in frequency and how thick the ice in the lead can be) between different remote sensing approaches (von Albedyll et al., 2022). Thus, direct and absolute comparison of lead retrievals can be difficult for different products and resolutions. Nevertheless, the same physical principles (like the power law correspondence) are valid for different scales and resolutions (Wernecke and Kaleschke, 2015). We recommend that any lead width study should check if the power law scaling conditions are fulfilled to increase confidence in the validity of the obtained results.

7. Conclusions

On a local (5–10 km) and regional (20–40 km) scale, we investigate the variation of the surface temperatures in time and space and derived lead properties. Along the MOSAiC drift during the winter season, we use high resolution surface temperature maps obtained from helicopter flights to examine small-scale lead properties. First, we investigated the surface temperatures and found: (i) its temporal variability is influenced by meteorological changes, such as warm air intrusions, often associated with high wind speeds, and (ii) its spatial variability over thick ice decreases as wind speed increases. For each flight, we retrieve classified lead maps and lead area fractions, based on a lead classification applied to the surface temperature maps using a dynamic temperature threshold. We see a high variability of the local lead area fraction and the influence of events, like the November 2019 storm. On a regional scale, there is a more stable lead area fraction evolution between 0% and 1% (until January), followed by an increase to 4% (March). This evolution agrees well with other MOSAiC studies on the regional scale. From the classified lead maps, we additionally determine lead width and orientation for all lead segments of every flight. This reveals three main findings: 1) the lead width distribution follows a power law (Equation 1) with an exponent of b=2.63 (narrow leads dominate wide leads), which is consistent with previous research, 2) the power law exponent increases in the course of the winter, 3) small-scale leads typically have one primary orientation. However, that orientation changes between the flights and throughout the winter season and

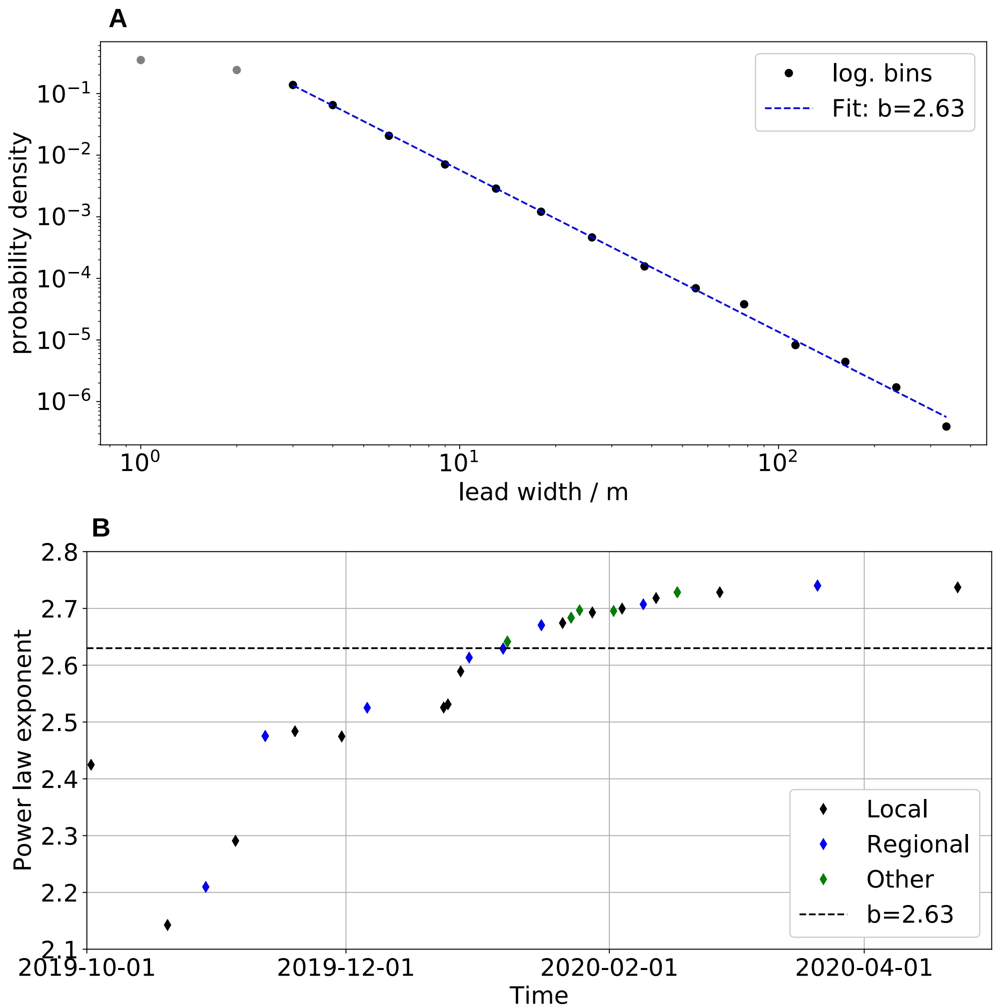

Figure 9. Lead width distribution with the power law fit for all and single flights.

(A) The logarithmic frequencies of the lead widths of all 35 flights combined, also binned logarithmic, are represented as black points. The blue dashed line shows the negative power law fit exponent b=2.63. The power law fit is constrained to the lead width $\geq$ 3 m. (B) Time series of the power law exponent for all 35 flights between 02 October 2019 and 23 April 2020; in black for local flight, in blue for regional flights, and in green for other flight types. The horizontal line marks the exponent of all flights (2.63) from (A).

no overall prevailing orientation is found. The abundance of small scale leads emphasises the necessity to understand their physical processes better, where our high spatial resolution data can help. However, those narrow leads are not individually included in the current thermal infrared satellite data of about 1 km resolution (e.g., MODIS). We suggest a representation of the smallest leads on the satellite sub-footprint scale because the heat transfer is not linear with surface temperature. In fact, the heat exchange is larger for leads within thick sea ice compared to larger areas of uniformed thinner sea ice with the same average surface temperature. Such parameterizations could also improve model simulation for considering small scale lead processes.

Beyond this study, we plan to perform a one-to-one comparison of the high-resolution helicopter-borne data with thermal infrared satellite data, e.g., MODIS ice surface temperatures. The aim is to assess how well the lead's impact on the atmosphere is represented in the satellite retrieval. Additionally, comparisons with the deformation rate from buoy grids on different scales or inter-comparison with helicopter-borne topography data can be used to understand the MOSAiC lead characteristics better.

References

Alfred-Wegener-Institut Helmholtz-Zentrum für Polar- und Meeresforschung. 2017. Polar Research and Supply Vessel POLARSTERN operated by the Alfred-Wegener-Institute. *Journal of large-scale research facilities* **3**. doi:http://dx.doi.org/10.17815/jlsrf-3-163.

Bintanja R, Van Der Linden EC. 2013. The changing seasonal climate in the Arctic. *Scientific Reports* **3**: 1–8. ISSN 20452322. doi:https://doi.org/10.1038/srep01556.

Bröhan D, Kaleschke L. 2014. A nine-year climatology of arctic sea ice lead orientation and frequency from AMSR-E. *Remote Sensing* **6**(2): 1451–1475. doi:10.3390/rs6021451.

Burger W, Burge MJ. 2009. *Undergraduate Topics in Computer Science. Principles of Digital Image Processing. Core Algorithms*. Springer-Verlag London. doi:https://doi.org/10.1007/978-1-84800-195-4.

Cox C, Gallagher M, Shupe M, Persson O, Solomon A, et al. 2021. 10-meter (m) meteorological flux tower measurements (Level 1 Raw), Multidisciplinary Drifting Observatory for the Study of Arctic Climate (MOSAiC), central Arctic, October 2019 - September 2020 [dataset]. *Arctic Data Center* https://doi.org/10.18739/A2VM42Z5F.

Dai A, Luo D, Song M, Liu J. 2019. Arctic amplification is caused by sea-ice loss under increasing CO_2. *Nature communications* **10**(1): 1–13. doi:https://doi.org/10.1038/s41467-018-07954-9.

Dethloff K, Maslowski W, Hendricks S, Lee YJ, Goessling HF, et al. 2022. Arctic sea ice anomalies during the MOSAiC winter 2019/20. *The Cryosphere* **16**(3): 981–1005. doi:10.5194/tc-16-981-2022. https://tc.copernicus.org/articles/16/981/2022/.

Fox-Kemper B, et al. 2021. The Physical Science Basis. Contribution of Working Group I to the Sixth Assessment Report of the Intergovernmental Panel on Climate Change: Ocean, Cryosphere and Sea Level Change. *Climate change* .

Guo W, Itkin P, Singha S, Paul Doulgeris A, Johansson M, et al. 2022. Sea ice classification of TerraSAR-X ScanSAR images for the MOSAiC expedition incorporating per-class incidence angle dependency of image texture. *The Cryosphere Discussions* **2022**: 1–29. doi:https://doi.org/10.5194/tc-2022-86.

Hutter N, Bouchat A, Dupont F, Dukhovskoy D, Koldunov N, et al. 2022. Sea Ice Rheology Experiment (SIREx): 2. Evaluating Linear Kinematic Features in High-Resolution Sea Ice Simulations. *Journal of Geophysical Research: Oceans* **127**(4). doi:https://doi.org/10.1029/2021JC017666.

Hutter N, Losch M, Menemenlis D. 2018. Scaling Properties of Arctic Sea Ice Deformation in a High-Resolution Viscous-Plastic Sea Ice Model and in Satellite Observations. *Journal of Geophysical Research: Oceans* **123**(1): 672–687. doi:https://doi.org/10.1002/2017JC013119.

Ivanova N, Rampal P, Bouillon S. 2016. Error assessment of satellite-derived lead fraction in the Arctic. *Cryosphere* **10**(2): 585–595. doi:https://doi.org/10.5194/tc-10-585-2016.

Kortum K, Singha S, Spreen G. 2022. Robust Multiseasonal Ice Classification From High-Resolution X-Band SAR. *IEEE Transactions on Geoscience and Remote Sensing* **60**: 1–12. doi:https://doi.org/10.1109/TGRS.2022.3144731.

Krumpen T, Birrien F, Kauker F, Rackow T, Albedyll Lv, et al. 2020. The MOSAiC ice floe: sediment-laden survivor from the Siberian shelf. *The Cryosphere* **14**(7): 2173–2187. doi:https://doi.org/10.5194/tc-14-2173-2020.

Krumpen T, von Albedyll L, Goessling HF, Hendricks S, Juhls B, et al. 2021. MOSAiC drift expedition from October 2019 to July 2020: Sea ice conditions from space and comparison with previous years. *The Cryosphere* **15**(8): 3897–3920. doi:https://doi.org/10.5194/tc-15-3897-2021.

Kwok R. 2018. Arctic sea ice thickness, volume, and multiyear ice coverage: Losses and coupled variability (1958-2018). *Environmental Research Letters*

13(10). doi:https://doi.org/10.1088/1748-9326/aae3ec.

Kwok R, Spreen G, Pang S. 2013. Arctic sea ice circulation and drift speed: Decadal trends and ocean currents. *Journal of Geophysical Research: Oceans* **118**(5): 2408–2425. doi:https://doi.org/10.1002/jgrc.20191.

Lindsay R, Rothrock D. 1995. Arctic sea ice leads from advanced very high resolution radiometer images. *Journal of Geophysical Research: Oceans* **100**(C3): 4533–4544. doi:https://doi.org/10.1029/94JC02393.

Lüpkes C, Vihma T, Bimbaum G, Wacker U. 2008. Influence of leads in sea ice on the temperature of the atmospheric boundary layer during polar night. *Geophysical Research Letters* **35**(3): 2–6. ISSN 00948276. doi:https://doi.org/10.1029/2007GL032461.

Marcq S, Weiss J. 2012. Influence of sea ice lead-width distribution on turbulent heat transfer between the ocean and the atmosphere. *Cryosphere* **6**(1): 143–156. doi:https://doi.org/10.5194/tc-6-143-2012.

Masson-Delmotte V, Zhai P, Pirani A, Connors S, Péan C, et al. 2021. IPCC, 2021: Climate Change 2021: The Physical Science Basis. Contribution of Working Group I to the Sixth Assessment Report of the Intergovernmental Panel on Climate Change.

Maykut GA. 1978. Energy exchange over young sea ice in the central Arctic. *Journal of Geophysical Research: Oceans* **83**(C7): 3646–3658. doi:https://doi.org/10.1029/JC083iC07p03646.

Maykut GA. 1982. Large-Scale Heat Exchange and Ice Production in the Central Arctic. *Journal of Geophysical Research* **87**(C10): 7971–7984. doi:https://doi.org/10.1029/JC087iC10p07971.

Meredith M, Sommerkorn M, Cassotta S, Derksen C, Ekaykin A, et al. 2019. Polar Regions. Chapter 3, IPCC Special Report on the Ocean and Cryosphere in a Changing Climate. *IPPC* .

Muchow M, Schmitt AU, Kaleschke L. 2021. A lead-width distribution for Antarctic sea ice: a case study for the Weddell Sea with high-resolution Sentinel-2 images. *The Cryosphere* **15**(9): 4527–4537. doi:https://doi.org/10.5194/tc-15-4527-2021.

Najman L, Schmitt M. 1994. Watershed of a continuous function. *Signal Processing* **38**(1): 99–112. doi:https://doi.org/10.1016/0165-1684(94)90059-0.

Nandan V, Willatt R, Mallett R, Stroeve J, Geldsetzer T, et al. 2022. Wind Transport of Snow Impacts Ka- and Ku-band Radar Signatures on Arctic Sea Ice. *The Cryosphere Discussions* **2022**: 1–38. doi:10.5194/tc-2022-116.

Nicolaus M, Perovich DK, Spreen G, Granskog MA, von Albedyll L, et al. 2022.

Overview of the MOSAiC expedition: Snow and sea ice. *Elem Sci Anth* **10**(1): 000046. doi:https://doi.org/10.1525/elementa.2021.000046.
Nixdorf U, Dethloff K, Rex M, Shupe M, Sommerfeld A, et al. 2021. MOSAiC extended acknowledgement. *Zenodo* https://doi.org/10.5281/zenodo.5541624.
Qu M, Pang X, Zhao X, Zhang J, Ji Q, et al. 2019. Estimation of turbulent heat flux over leads using satellite thermal images. *The Cryosphere* **13**(6): 1565–1582. doi:https://doi.org/10.5194/tc-13-1565-2019.
Rabe B, Heuzé C, Regnery J, Aksenov Y, Allerholt J, et al. 2022. Overview of the MOSAiC expedition: Physical oceanography. *Elem Sci Anth* **10**(1): 00062. doi:https://doi.org/10.1525/elementa.2021.00062.
Rampal P, Weiss J, Marsan D. 2009. Positive trend in the mean speed and deformation rate of Arctic sea ice, 1979-2007. *Journal of Geophysical Research: Oceans* **114**(5). doi:https://doi.org/10.1029/2008JC005066.
Ridler T, Calvard S, et al. 1978. Picture thresholding using an iterative selection method. *IEEE trans syst Man Cybern* **8**(8): 630–632. doi:https://doi.org/10.1109/TSMC.1978.4310039.
Ringeisen D, Hutter N, von Albedyll L. 2022. Deformation lines in Arctic sea ice: intersection angles distribution and mechanical properties. *EGUsphere* pp. 1–22. doi:10.5194/egusphere-2022-1481.
Ringeisen D, Losch M, Bruno Tremblay L, Hutter N. 2019. Simulating intersection angles between conjugate faults in sea ice with different viscous-plastic rheologies. *Cryosphere* **13**(4): 1167–1186. doi:https://doi.org/10.5194/tc-13-1167-2019.
Ringeisen D, Tremblay LB, Losch M. 2021. Non-normal flow rules affect fracture angles in sea ice viscous-plastic rheologies. *Cryosphere* **15**(6): 2873–2888. doi:https://doi.org/10.5194/tc-15-2873-2021.
Rinke A, Cassano JJ, Cassano EN, Jaiser R, Handorf D. 2021. Meteorological conditions during the MOSAiC expedition. *Elementa: Science of the Anthropocene* **9**(1). doi:https://doi.org/10.1525/elementa.2021.00023. https://online.ucpress.edu/elementa/article/9/1/00023/118092/Meteorological-conditions-during-the-MOSAiC.
Schulson EM. 2004. Compressive shear faults within arctic sea ice: Fracture on scales large and small. *Journal of Geophysical Research C: Oceans* **109**(7). doi:https://doi.org/10.1029/2003JC002108.
Serreze MC, Barrett AP, Stroeve JC, Kindig DN, Holland MM. 2009. The emergence of surface-based Arctic amplification. *Cryosphere* **3**(1): 11–19.

ISSN 19940424. doi:https://doi.org/10.5194/tc-3-11-2009.
Serreze MC, Barry RG. 2011. Processes and impacts of Arctic amplification: A research synthesis. *Global and Planetary Change* **77**(1): 85–96. ISSN 0921-8181. doi:https://doi.org/10.1016/j.gloplacha.2011.03.004.
Shokr M, Sinha N. 2015. *Sea ice: physics and remote sensing*. John Wiley & Sons.
Shupe MD, Rex M, Blomquist B, Persson POG, Schmale J, et al. 2022. Overview of the MOSAiC expedition: Atmosphere. *Elem Sci Anth* **10**(1): 00060. doi:https://doi.org/10.1525/elementa.2021.00060.
Shupe MD, Rex M, Dethloff K, Damm E, Fong A, et al. 2020. Arctic Report Card 2020: The MOSAiC Expedition: A Year Drifting with the Arctic Sea Ice. *NOAA* doi:https://doi.org/10.25923/9g3v-xh92.
Spreen G, Kern S. 2017. Methods of satellite remote sensing of sea ice, in *Sea ice / edited by David N. Thomas*. John Wiley & Sons: Chap. 9.
Spreen G, Kwok R, Menemenlis D. 2011. Trends in Arctic sea ice drift and role of wind forcing: 1992-2009. *Geophysical Research Letters* **38**(19): 1–6. doi:https://doi.org/10.1029/2011GL048970.
Tetzlaff A, Lüpkes C, Hartmann J. 2015. Aircraft-based observations of atmospheric boundary-layer modification over Arctic leads. *Quarterly Journal of the Royal Meteorological Society* **141**(692): 2839–2856. doi:https://doi.org/10.1002/qj.2568.
Thielke L, Huntemann M, Hendricks S, Jutila A, Ricker R, et al. 2022. Helicopter-borne thermal infrared sea ice surface temperature maps with 1 m resolution during the MOSAiC expedition, NetCDF format, version 3 [dataset]. *PANGAEA* https://doi.org/10.1594/PANGAEA.950683.
Thielke L, Huntemann M, Hendricks S, Jutila A, Ricker R, et al. 2022. Sea ice surface temperatures from helicopter-borne thermal infrared imaging during the MOSAiC expedition. *Scientific Data* **9**(1): 1–16. doi:https://doi.org/10.1038/s41597-022-01461-9.
Thielke L, Huntemann M, Spreen G. 2022. Lead classification maps from helicopter-borne surface temperatures with 1 m resolution during the MOSAiC expedition [dataset]. *PANGAEA* https://doi.org/10.1594/PANGAEA.951568.
Tschudi MA, Curry JA, Maslanik JA. 2002. Characterization of springtime leads in the Beaufort/Chukchi seas from airborne and satellite observations during FIRE/SHEBA. *Journal of Geophysical Research: Oceans* **107**(10). doi:https://doi.org/10.1029/2000jc000541.
Vihma T, Pirazzini R. 2005. On the factors controlling the snow

surface and 2-m air temperatures over the Arctic sea ice in winter. *Boundary-Layer Meteorology* **117**(1): 73–90. doi:https://doi.org/10.1007/s10546-004-5938-7.

Vihma T, Pirazzini R, Fer I, Renfrew IA, Sedlar J, et al. 2014. Advances in understanding and parameterization of small-scale physical processes in the marine Arctic climate system: a review. *Atmospheric Chemistry and Physics* **14**(17): 9403–9450. doi:https://doi.org/10.5194/acp-14-9403-2014.

von Albedyll L, et al. 2022. Lead fractions from SAR-derived sea ice divergence during MOSAiC. *In preparation* .

Wadhams P. 1981. Sea-ice topography of the Arctic Ocean in the region 70 W to 25 E. *Philosophical Transactions of the Royal Society of London Series A, Mathematical and Physical Sciences* **302**(1464): 45–85. doi:https://doi.org/10.1098/rsta.1981.0157.

Wadhams P, McLaren AS, Weintraub R. 1985. Ice thickness distribution in Davis Strait in February from submarine sonar profiles. *Journal of Geophysical Research: Oceans* **90**(C1): 1069–1077. doi:https://doi.org/10.1029/JC090iC01p01069.

Wang Q, Danilov S, Jung T, Kaleschke L, Wernecke A. 2016. Sea ice leads in the Arctic Ocean: Model assessment, interannual variability and trends. *Geophysical Research Letters* **43**(13): 7019–7027. ISSN 19448007. doi:https://doi.org/10.1002/2016GL068696.

Wang S, Wang Q, Jordan RE, Persson PO. 2001. Interactions among longwave radiation of clouds, turbulence, and snow surface temperature in the Arctic: A model sensitivity study. *Journal of Geophysical Research Atmospheres* **106**(D14): 15323–15333. ISSN 01480227. doi:https://doi.org/10.1029/2000JD900358.

Wendisch M, Brückner M, Burrows J, Crewell S, Dethloff K, et al. 2017. Understanding causes and effects of rapid warming in the Arctic. *Eos* **98**. doi:http://dx.doi.org/10.1029/2017EO064803.

Wernecke A, Kaleschke L. 2015. Lead detection in Arctic sea ice from CryoSat-2: Quality assessment, lead area fraction and width distribution. *Cryosphere* **9**(5): 1955–1968. doi:https://doi.org/10.5194/tc-9-1955-2015.

Willmes S, Heinemann G. 2015. Pan-arctic lead detection from MODIS thermal infrared imagery. *Annals of Glaciology* **56**(69): 29–37. ISSN 02603055. doi:https://doi.org/10.3189/2015AoG69A615.

Willmes S, Heinemann G. 2016. Sea-ice wintertime lead frequencies and regional characteristics in the Arctic, 2003-2015. *Remote Sensing* **8**(1): 2003–2015. ISSN 20724292. doi:https://doi.org/10.3390/rs8010004.

WMO. 2014. SEA ICE NOMENCLATURE. https://library.wmo.int/index.php?lvl=notice_display&id=6772, lastaccessFebruary16,2022.

Yu Y, Rothrock DA. 1996. Thin ice thickness from satellite thermal imagery. *Journal of Geophysical Research C: Oceans* **101**(C11): 25753–25766. doi:https://doi.org/10.1029/96JC02242.

Contributions

Contributed to conception and design: LT, GS, MH
Contributed to acquisition of data: LT, GS, MH
Contributed to analysis and interpretation of data: all authors
Drafted the article: LT
Revised the article: all authors
Approved the submitted version for publication: all authors

Acknowledgments

This work was supported by the German Ministry for Education and Research (BMBF) as part of the International Multidisciplinary drifting Observatory for the Study of the Arctic Climate (grant MOSAiC20192020), and IceSense (grant 03F0866B). We acknowledge the support by the Deutsche Forschungsgemeinschaft (DFG) through the International Research Training Group IRTG 1904 ArcTrain (grant 221211316), the MOSAiCmicrowaveRS project (grant 420499875), and the Transregional Collaborative Research Center TRR 172 (grant 268020496) "Arctic Amplification: Climate Relevant Atmospheric and Surface Processes, and Feedback Mechanisms $(AC)^3$". We thank all persons who contributed to the expedition of the Research Vessel Polarstern during MOSAiC in 2019-2020 (AWI_PS122_00) (Nixdorf et al., 2021), and especially, HeliService and their pilots. Without them, the helicopter survey flights and the collection of the data would not have been possible. We thank Janna Rückert for the discussions about this the manuscript.

Competing interests

The authors have no competing interests, as defined by Elementa, that might be perceived to influence the research presented in this manuscript.

Data accessibility statement

- Helicopter-borne surface temperature maps, 1 m resolution: (Thielke et al., 2022).
- Lead classification maps, 1 m resolution: (Thielke et al., 2022)
- Atmospheric in-situ data: Cox et al. (2021) [updated version used]